

## Research Article

# Research on Dynamic Response of Concrete-Filled Steel Tube Columns Confined with FRP under Blast Loading

Jing Dong , Junhai Zhao , Dongfang Zhang , and Yingping Li

*School of Civil Engineering, Chang'an University, Xi'an, Shaanxi 710061, China*

Correspondence should be addressed to Junhai Zhao; zhaojh@chd.edu.cn

Received 8 January 2019; Revised 6 June 2019; Accepted 20 June 2019; Published 10 July 2019

Academic Editor: Chao Tao

Copyright © 2019 Jing Dong et al. This is an open access article distributed under the Creative Commons Attribution License, which permits unrestricted use, distribution, and reproduction in any medium, provided the original work is properly cited.

Recently, a concrete-filled steel tube confined with fiber-reinforced polymer (FRP) has become a hot research issue as a new type of structure. These studies mainly focus on its static performance and seismic and impact behaviour, with little research on its blast resistance performance. In this study, the dynamic response of concrete-filled steel tube columns confined with FRP under blast loading was investigated. Numerical analysis was implemented using multimaterial ALE method in the finite element analysis program LS-DYNA. The proposed numerical model was validated by the SDOF result and available experimental data. And the effects of the number of FRP layers, concrete strength, and cross section were also discussed in detail based on the proposed numerical model. The results indicate that the constraints of FRP effectively enhance the blast resistance of the column, and the vulnerable parts mainly occur at the middle and two ends of the column. The blast resistance of the column can be enhanced by increasing the number of FRP layers or concrete strength. These results could provide a certain basis for blast resistance design of concrete-filled steel tubes confined with FRP.

## 1. Introduction

In recent years, accidents caused by explosions occurred frequently. It has become an important and urgent task to prevent the structural damage and collapse of buildings under blast loading. Therefore, it is of great significance to research the dynamic response, failure modes, and damage mechanisms of building structures to improve the blast resistance performance of these structures and reduce accident losses. Concrete-filled steel tubes (CFSTs) have widely been studied and applied in civil engineering as a classical composite structure. A concrete-filled steel tube has the advantages of ease of construction, high bearing capacity, and excellent ductility [1–3]. However, in some high corrosive environments, corrosion protection of the steel tube is required, which increases the maintenance costs. Fiber-reinforced polymer (FRP) is a high-performance composite material which is composed of certain proportions of fiber material and resin matrix material. FRP has widely been used in engineering practice due to its high strength-to-weight ratios and corrosion resistance [4, 5]. Recently, a new type of structure based on CFST, CFST confined with FRP,

has been proposed. CFST column confined with FRP is a composite structure of an FRP composite material and concrete-filled steel tube (Figure 1). When the concrete is confined to the steel tube, FRP is wrapped around the whole steel tube. On the one hand, the CFST column confined with FRP can be used as a new type of structure in new buildings. On the other hand, the FRP material can also be used as a repair material to reinforce existing CFST structures.

Xiao et al. [6] proposed the concept of a confined concrete-filled steel tube column on the basis of concrete-filled steel tube. Taking CFST columns confined with carbon fiber-reinforced polymer (CFRP) as an example, an axial compression test and a seismic test were carried out. The test results showed that the axial bearing capacity and seismic performance of CFST columns confined with CFRP were significantly improved compared to the traditional CFST column. This new structure could be used in high-rise buildings and bridges in seismic areas. Later, many researchers focused on the ultimate bearing capacity and working mechanisms, and compression and bending experiments were implemented [7–14]. The results showed that the bearing capacity and stiffness of CFST columns

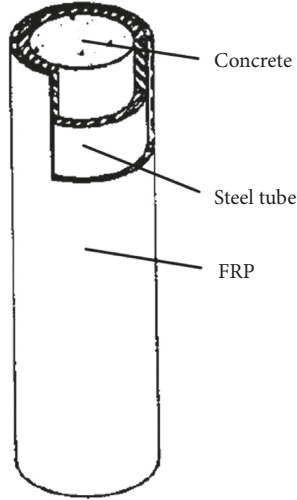


FIGURE 1: Concrete-filled steel tube confined with FRP.

confined with FRP were greatly improved compared with CFST columns. As to the studies on CFST columns confined with FRP under impulsive load, Alam et al. [15, 16] and Chen et al. [17] carried out lateral impact tests and numerical simulation. The deflection and impact force were observed, and the effect of impact velocity, vehicle mass, and FRP thickness was investigated. The results indicated that using FRP could reduce the maximum and residual displacement. Nevertheless, there is little research on the dynamic response of concrete-filled steel tube columns confined with FRP under blast loading. Although the blast load is also a type of impulsive load, the strain rate under seismic load and impact load is  $10^{-3} \sim 10^{-1} \text{ s}^{-1}$  and  $10^{-2} \sim 10^1 \text{ s}^{-1}$ , respectively, while the strain rate under blast load is within the range from  $10^2$  to  $10^6 \text{ s}^{-1}$  [18]. Thus, the blast response of CFST columns confined with FRP still needs to be investigated.

The explosion of a structure is a typical nonlinear transient dynamic issue. It is quite difficult to solve the problem of explosion mechanics using theoretical analysis methods. The experimental method not only is expensive but also cannot reflect the state of the explosion process. Numerical simulations can greatly save experimental expenses and can also observe the data and phenomena that cannot be obtained in experiments. Numerical simulation is consequently often used in the research of structural blast resistance [19]. Mutalib and Hao [20] modelled an FRP-strengthened reinforced concrete panel with additional anchorages against blast loads and analysed the dynamic response of FRP-strengthened reinforced concrete wall with different anchorage systems. Mao et al. [21] modelled an ultrahigh performance fiber-reinforced concrete panel under blast loading. The strain rate effect of the material was taken into account in the model. Zhang et al. [22] modelled concrete-filled steel tube columns under static and blast loads. The numerical results indicated that the CFST columns showed good flexural behaviour under both static and dynamic loads. In the aforementioned studies, the numerical results showed a good agreement with the corresponding experimental results, which validated the reliability of the numerical model.

In this study, the dynamic response of CFST columns confined with FRP under blast loading is investigated. In Section 2, a finite element (FE) model is developed using the arbitrary Lagrange–Euler (ALE) method. In Section 3, the validation of the proposed model is presented. In Section 4, the numerical results and parameter study are discussed. Conclusions are described in Section 5.

## 2. FE Model of CFST Column Confined with FRP

LS-DYNA is a well-known explicit dynamic analysis program and is one of the most commonly used software programs for numerical simulations of blast performance of structures. In this study, the g-mm-ms-MPa unit system is adopted in modelling, and a typical CFST column confined with FRP under blast loading is modelled using the commercial software ANSYS/LS-DYNA.

**2.1. Description of Model.** The column is 3000 mm high, the outer diameter of the steel tube is 500 mm, the diameter of the core concrete is 480 mm, and the thickness of the steel tube is 10 mm. The CFST column is wrapped by using a CFRP sheet with a thickness of 0.167 mm. Both ends of the column are constrained. The explosive is 300 mm × 300 mm × 300 mm TNT (mass equivalent to 44.28 kg). The scaled distance is  $z = L/\sqrt[3]{M} = 0.28 \text{ m/kg}^{1/3}$ . The size of the air domain is 2500 mm × 2000 mm × 3600 mm. The TNT, air, steel tube, and concrete are all solid elements, and the FRP is composed of shell elements. The front view and the top view of the model are shown in Figure 2, and the completed 3D finite element model is shown in Figure 3.

### 2.2. Material Models

**2.2.1. Material Model and Equation of State for Air.** Material type 9 (MAT\_NULL) in LS-DYNA was used to model the air, and EOS type 1 (EOS\_LINEAR\_POLYNOMIAL) was chosen to define the linear polynomial equation of state of air. The pressure is given by [23]

$$P = C_0 + C_1\mu + C_2\mu^2 + C_3\mu^3 + (C_4 + C_5\mu + C_6\mu^2)E, \quad (1a)$$

$$\mu = \frac{1}{V} - 1, \quad (1b)$$

where  $P$  is the pressure,  $C_0 \sim C_6$  are the polynomial equation coefficients,  $V$  is the relative volume, and  $E$  is the internal energy per unit reference specific volume. When simulating air, the main variables and values are shown in Table 1.

**2.2.2. Material Model and Equation of State for TNT.** Material type 8 (MAT\_HIGH\_EXPLOSIVE\_BURN) in LS-DYNA was used to model TNT. This model is particularly suitable for modelling the detonation of a high explosive. The JWL (EOS\_JWL) equation was used to define the equation of state for TNT. The JWL equation of state defines the pressure as

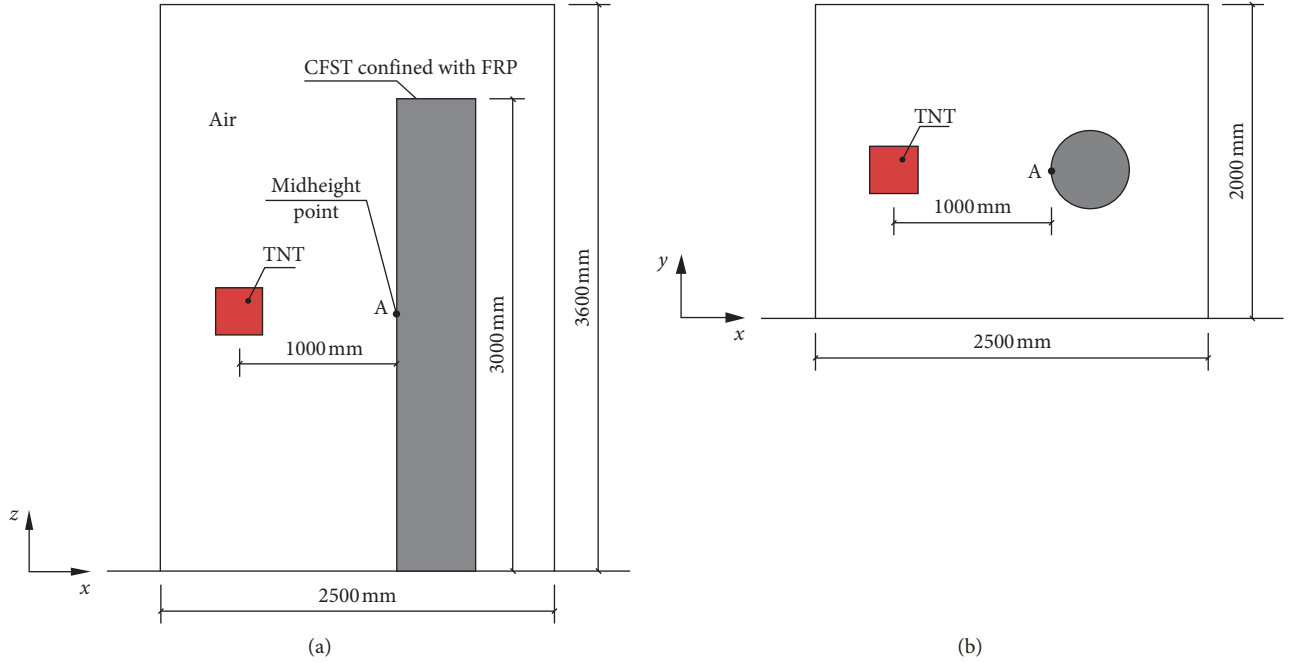


FIGURE 2: Model of the CFST column confined with FRP under blast loading. (a) Front view. (b) Top view.

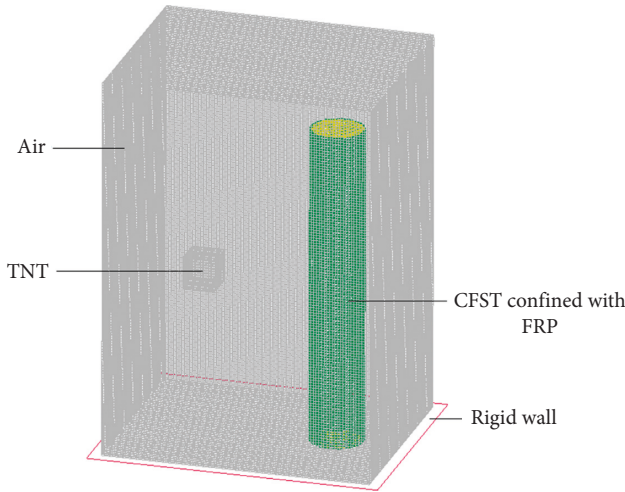


FIGURE 3: 3D finite element model.

TABLE 1: Variables of air.

Variable	Density	$C_0$	$C_1$	$C_2$	$C_3$	$C_4$	$C_5$	$C_6$	$E_0$
Unit	$\text{g/mm}^3$	—	—	—	—	—	—	—	$\text{J/mm}^3$
Value	$1.29 \times 10^{-6}$	0	0	0	0	0.4	0.4	0	0.25

$$p = A \left( 1 - \frac{\omega}{R_1 V} \right) e^{-R_1 V} + B \left( 1 - \frac{\omega}{R_2 V} \right) e^{-R_2 V} + \frac{\omega E}{V}, \quad (2)$$

where  $p$  is the explosive pressure;  $V$  is the relative volume;  $E_0$  is the initial internal energy per unit reference specific volume and  $\omega$ ;  $A$ ,  $B$ ,  $R_1$ , and  $R_2$  are the material constants. When simulating TNT, the main variables and values are

shown in Table 2, where  $D$  refers to the detonation velocity and PCJ represents the Chapman–Jouguet pressure.

**2.2.3. Material Model for Steel Tube.** Material type 3 (MAT\_PLASTIC\_KINEMATIC) in LS-DYNA was used to represent the steel tube. This model is a kinematic hardening plasticity model considering the strain rate effect, which is suitable for simulating steel material with a high strain rate. This material model is based on the Cowper–Symonds model. The yield stress is given by [24]

$$\sigma_y = \left[ 1 + \left( \frac{\dot{\epsilon}}{C} \right)^{1/p} \right] (\sigma_0 + \beta E_p \epsilon_p^{\text{eff}}), \quad (3)$$

where  $\dot{\epsilon}$  is the strain rate,  $C$  and  $p$  are the strain rate parameters,  $\sigma_0$  is the initial yield stress,  $\beta$  is the hardening parameter (for kinematic hardening,  $\beta = 0$ ; for isotropic hardening,  $\beta = 1$ ),  $E_p$  is the plasticity hardening modulus, and  $\epsilon_p^{\text{eff}}$  is the effective plastic strain. In this paper, the variable values of steel are listed in Table 3.

**2.2.4. Material Model for Concrete.** Concrete was modelled using the material type 111 (MAT\_JOHNSON\_HOLMQUIST\_CONCRETE) in LS-DYNA. This model could be applied to simulate the concrete material under high strain, high strain rate, and high pressure. The Johnson–Holmquist–Cook model is a rate-dependent damage constitutive model proposed by Holmquist et al. [25]. The equivalent yield strength is given by

$$\sigma^* = [A(1-D) + Bp^{*N}] \left[ 1 + C \ln \left( \frac{\dot{\epsilon}}{\dot{\epsilon}_0} \right) \right], \quad (4a)$$

TABLE 2: Variables of TNT.

Variable	Density	$D$	PCJ	$A$	$B$	$R_1$	$R_2$	$E_0$
Unit	$\text{g}/\text{mm}^3$	$\text{mm}/\text{ms}$	MPa	MPa	MPa	—	—	$\text{J}/\text{mm}^3$
Value	$1.64 \times 10^{-3}$	6930	$2.1 \times 10^5$	$3.74 \times 10^5$	3230	4.15	0.95	7000

TABLE 3: Variables of the steel material model.

Variable	RO	$E$	PR	SIGY	ETAN	BETA	SRC	SRP	FS	VP
Unit	$\text{g}/\text{mm}^3$	MPa	—	MPa	MPa	—	—	—	—	—
Value	$7.83 \times 10^{-3}$	$2.08 \times 10^5$	0.3	292.5	2100	0	40	5	0.25	—

RO: mass density;  $E$ : Young's modulus; PR: Poisson's ratio; SIGY: yield stress; ETAN: tangent modulus; BETA: hardening parameter; SRC and SRP: strain rate parameters; FS: effective plastic strain for eroding elements; VP: formulation for rate effects.

where  $\sigma^* = \sigma/f_c$  is the normalized equivalent stress;  $p^* = p/f_c$  is the normalized pressure;  $\dot{\epsilon}$  is the strain rate;  $\dot{\epsilon}_0 = 1.0 \text{ s}^{-1}$  is the reference strain rate; and  $A$ ,  $B$ ,  $C$ , and  $N$  are the normalized cohesive strength, normalized pressure hardening, strain rate coefficient, and pressure hardening exponent, respectively.  $D$  represents the damage parameter and is expressed as [26]

$$D = \sum \frac{\Delta \epsilon_p + \Delta \mu_p}{\epsilon_p^f + \mu_p^f} = \sum \frac{\Delta \epsilon_p + \Delta \mu_p}{D_1 (p^* + T^*)^{D_2}}, \quad (4b)$$

where  $\Delta \epsilon_p$  and  $\Delta \mu_p$  are the equivalent plastic strain and plastic volumetric strain,  $T^* = T/f_c$  denotes the normalized maximum tensile hydrostatic pressure, and  $D_1$  and  $D_2$  are the material damage constants.

The Johnson–Holmquist–Cook model takes into account the effects of large strain, high strain rate, and damage accumulation of concrete. It can describe the mechanical behaviour of concrete under explosion and high-speed impact and penetration [27]. In this paper, the variable values of the concrete are shown in Table 4.

**2.2.5. Material Model for FRP.** A linear elastic material model (MAT\_ELASTIC) was used to simulate FRP. FRP sheets can be considered to be in the elastic stage before breakage, so its constitutive relation can be simulated by the linear elastic stress-strain relation [28, 29]. In this paper, the variable values of FRP are listed in Table 5.

**2.3. Strain Rate Effect.** The dynamic behaviour of the concrete material is strain rate dependent. Both the compressive and tensile strengths vary with the strain rate. Recommended by Committee Euro-International du Béton (CEB), the dynamic increase factor (DIF) is defined as the ratio of dynamic strength to static strength. For concrete in compression, the equation of DIF is given by [30]

$$\text{CDIF} = \frac{f_{cd}}{f_{cs}} = \begin{cases} \left( \frac{\dot{\epsilon}}{\dot{\epsilon}_s} \right)^{1.026\alpha}, & \dot{\epsilon} \leq 30 \text{ s}^{-1}, \\ \gamma \left( \frac{\dot{\epsilon}}{\dot{\epsilon}_s} \right)^{1/3}, & \dot{\epsilon} > 30 \text{ s}^{-1}, \end{cases} \quad (5)$$

where  $\dot{\epsilon}$  is the strain rate,  $\dot{\epsilon}_s = 3 \times 10^{-5} \text{ s}^{-1}$ ,  $\alpha = 1/(5 + 9f_{cs}/10)$ , and  $\lg \gamma = 6.156\alpha - 2$ .

For concrete in tension, the equation of DIF is given by

$$\text{TDIF} = \frac{f_{td}}{f_{ts}} = \begin{cases} \left( \frac{\dot{\epsilon}}{\dot{\epsilon}_s} \right)^\delta, & \dot{\epsilon} \leq 1 \text{ s}^{-1}, \\ \beta \left( \frac{\dot{\epsilon}}{\dot{\epsilon}_s} \right)^{1/3}, & \dot{\epsilon} > 1 \text{ s}^{-1}, \end{cases} \quad (6)$$

where  $\delta = 1/(1 + 8f_{cs}/10)$  and  $\lg \beta = 6\delta - 2$ .

The DIF for yield strength of steel is adopted by [31]

$$\text{DIF} = \frac{f_{yd}}{f_{ys}} = 1 + \left( \frac{\dot{\epsilon}}{C} \right)^{1/p}, \quad (7)$$

where  $C$  and  $p$  are the strain rate parameters mentioned above.

Compared with steel and concrete materials, the strain rate effect of FRP is insignificant [32]. Thus, the strain rate effect of FRP could be ignored in numerical simulations [33].

**2.4. Mesh Size.** When simulating the propagation of blast wave and its interaction with the structure, the accuracy of simulation results depends largely on the element mesh size. In order to find the most proper mesh size, the model of 44.28 kg TNT in the 3200 mm  $\times$  3200 mm  $\times$  3200 mm air domain was developed and the mesh size of 20 mm, 25 mm, 30 mm, and 50 mm was adopted for simulation, respectively. The overpressure values of the four models at different distances were compared with the empirical curve from UFC 3-340-02 [34]. As shown in Figure 4, the mesh size has certain influence on the peak overpressure of the shock wave. The accuracy of the numerical simulation performs better with the smaller mesh size. The overpressure value of 25 mm is close to the results of 20 mm. However, the computation amount and analysing time increase enormously than that of 25 mm, which leads to the risk of computer memory overflow. In addition, the simulation converged well when the mesh size is 25 mm. Therefore, the mesh size of 25 mm is employed in this paper for the dual consideration of simulation accuracy and computational efficiency.

**2.5. Generation of Blast Loading.** In LS-DYNA, there are three common ways to generate blast loading. The first way is to simplify the blast load, which is usually simplified to an

TABLE 4: Variables of the concrete material model.

Variable	RO	G	A	B	C	N	FC	T	EPS0	EFMIN	SFMAX	PC	UC	PL	UL	D <sub>1</sub>	D <sub>2</sub>	K <sub>1</sub>	K <sub>2</sub>	K <sub>3</sub>
Unit	g/mm <sup>3</sup>	MPa	—	—	—	—	MPa	MPa	ms <sup>-1</sup>	—	MPa	MPa	—	MPa	—	—	—	MPa	MPa	MPa
Value	$2.4 \times 10^{-3}$	14860	0.79	1.6	0.007	0.61	40	4	0.001	0.01	7	13	0.001	800	0.1	0.04	1	$8.5 \times 10^4$	$-1.71 \times 10^5$	$2.08 \times 10^5$

G: shear modulus; FC: quasi-static uniaxial compressive strength; T: maximum tensile hydrostatic pressure; EPS0: reference strain rate; EFMIN: plastic strain before fracture; SFMAX: normalized maximum strength; PC: crushing pressure; UC: crushing volumetric strain; PL: locking pressure; UL: locking volumetric strain; K<sub>1</sub>, K<sub>2</sub>, and K<sub>3</sub>: pressure constants.

TABLE 5: Variables of the FRP material model.

Variable	Density	Young's modulus	Poisson's ratio
Unit	$\text{g}/\text{mm}^3$	MPa	—
Value	$1.79 \times 10^{-3}$	$2.49 \times 10^5$	0.285

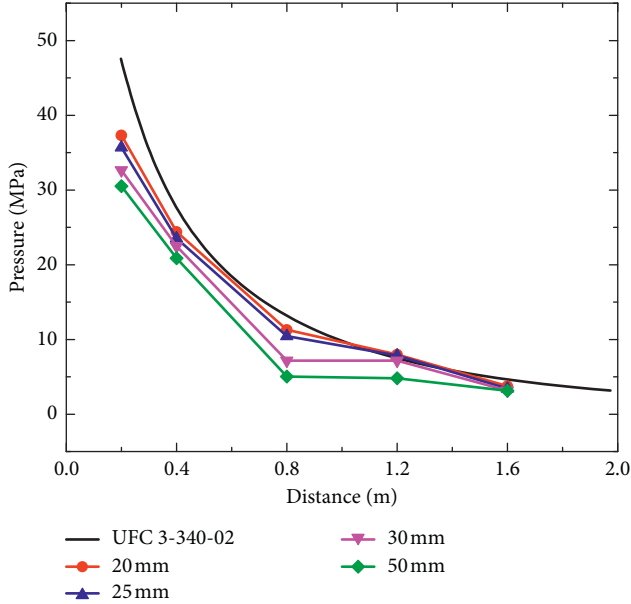


FIGURE 4: Comparison of different mesh sizes.

idealized triangular ramp pressure. The load curve is defined by the keyword \*LOAD\_CURVE in LS-DYNA. This method is simple in modelling, relatively high in computational efficiency, and suitable for dynamic response analysis of structural members with various distances. However, the accuracy of this method is relatively low, and it cannot simulate the propagation process of a blast wave. The second way utilizes the keyword \*LOAD\_BLAST in LS-DYNA to generate blast loading. This method requires inputting the equivalent mass of TNT, coordinates of detonation, type of blast, and other parameters in the keyword card. It has a wide application scope and the calculation results are relatively reasonable, but the shape of the explosive and the influence of obstacles on the structure cannot be taken into consideration. The third way is the fluid-structure coupling method, which requires establishing parts of air, explosive, and member. Multiple materials can be coupled by the arbitrary Lagrange-Euler (ALE) method. This method can accurately simulate the formation and propagation of the blast wave, and explosive shape and obstacles can be considered. The disadvantage of this method is that the modelling is rather complex. The computational efficiency is low due to the large computational amount. The third way, the ALE method, was applied in this study. By adding the \*INITIAL\_DETONATION keyword, the explosion is detonated at the center point of the TNT.

**2.6. Boundaries and Erosion.** With the consideration of reflection effect, a rigid plane was added to the bottom

surface of the air domain using the \*RIGIDWALL\_PLANAR keyword. The remaining surfaces of air domain were subjected to nonreflection boundaries. The fluid-structure interaction was processed using the \*CONSTRAINED\_LAGRANGE\_IN\_SOLID keyword. The nodes linked among steel tube, concrete, and FRP mesh were shared. The erosion algorithm was implemented using the \*MAT\_ADD\_EROSION keyword. Under the extreme loading, the element of material is deleted when it reaches a certain value. Based on the previous studies, a principle tensile strain of 0.001 is adopted to simulate the failure of concrete as the primary criterion in this study [35].

### 3. Verification of FE Model

The CFST column confined with FRP is a rapidly developed new type of composite material component in buildings recently. The references of blast tests for CFST column confined with FRP cannot be searched currently at home and abroad. Therefore, the finite element model of CFST column confined with FRP is not able to be verified directly by the relevant experiments. The accuracy and reliability of the abovementioned model was verified from three aspects, including the blast field tests of CFST column and reinforced concrete (RC) column with FRP and equivalent single-degree-of-freedom model, respectively. (1) The proposed FE model was verified against the blast tests of CFST columns in order to validate the developed model and the material models for air, TNT, steel tube, and concrete. And this situation was regarded as a special case when the FRP layer was 0. (2) To further verify the material model for FRP and ALE methods, the developed model was validated against the blast tests of RC columns confined with FRP. (3) A theoretical analysis on CFST column confined with FRP under blast loading was investigated to verify the dynamic response of numerical simulation. The FE model of the CFST column confined with FRP under blast loading precisely developed in this study was verified by the three above aspects. Based on the validated FE model, some exploratory researches were investigated and discussed.

**3.1. CFST Column Blast Test.** The blast field tests of three CFST columns and one concrete-filled double-skin steel tube column were carried out [36]. The steel tube was made of hot-rolled seamless steel and filled with C40 fine stone concrete. The specific specimen parameters are listed in Table 6, where  $H$  is the height of the column,  $D$  is the outside diameter of the steel tube,  $t$  is the thickness of the steel tube,  $M$  is the mass of TNT,  $H'$  is the height of TNT, and  $L$  is the distance between the TNT and the specimen.

This study performed numerical simulation verification on the test results of SC-1 and SC-2. A cube with dimensions of  $125 \text{ mm} \times 125 \text{ mm} \times 125 \text{ mm}$  was used to simulate 3 kg TNT explosive, and the air domain size was  $2500 \text{ mm} \times 1000 \text{ mm} \times 2500 \text{ mm}$ . Both ends of the CFST column were fixed, and displacement and rotation constraints were added.

TABLE 6: Parameters of the CFST column blast test.

Specimen	$H$ (mm)	$D$ (mm)	$t$ (mm)	$M$ (kg)	$H'$ (m)	$L$ (m)
SC-1	1800	273	7	3	0.9	1.6
SC-2	1800	273	7	50	0.9	0.7
SC-3	1800	273	7	50	0.9	8

Since the SC-1 test is a small-charge explosion test, there is no obvious damage phenomenon or displacement on SC-1. The experimental data of six measure points on the column SC-1 are compared with the numerical simulation results. As shown in Figure 5, the measure points #1, #2, #3, #4, #5, and #6 are set at the top, middle, and bottom of the front side and the back side of the column, respectively. Table 7 shows the comparison between the experimental and numerical data. It is found that all the numerical results are within 16% of the experimental value. The discrepancies at #3 and #6 are mainly caused by the site environment. The site of blast tests is an open and wide field, but the ground in simulation is modelled by using the limited rigid plane. This may affect the enhancement of overpressure reflection effect at the top of the column. Moreover, the results of blast tests are also influenced by incidental factors such as ideal air condition and climate. Even so, the distribution of simulation corresponds with experimental results and the overall discrepancy is within rational range.

The model of column SC-2 was generated using the same method as that of SC-1. A 350 mm × 300 mm × 300 mm cube was used to simulate 50 kg of TNT. Since this case was a close-in blast field, obvious damage of the specimen occurred.

Figure 6 displays the failure mode of column SC-2 under the close-in blast load of 50 kg TNT explosive. Figure 6(a) shows the experimental results, and Figure 6(b) shows the numerical results. By comparison, it can be seen that the numerical results are close to the experimental results, and obvious deformations in the middle of the column were observed in both test and numerical results. Figure 7 illustrates the displacement-time history curve of midheight point of column SC-2 in the numerical simulation. The maximum displacement of the middle-height point is 91.276 mm according to the figure, while the test result is 93 mm. The deviation rate is only 1.85%.

From the comparisons on parameters of the blast wave, it shows that the numerical results are in good agreement with the experimental results. As a result, the developed FE model can rationally reflect the dynamic response of CFST columns under blast loading. In other words, the generation of blast loading, material models, and state of equations for air and explosive in the proposed FE model are reasonable.

**3.2. RC Columns Confined with FRP Blast Test.** The field blast tests on eight RC pier columns with different protection were carried out by Liu [37]. Among the eight pier columns, specimen JS5 is an RC column wrapped with one layer of CFRP sheet. Blast tests were carried out under four different cases. The specific parameters of the four cases are listed in Table 8, where  $H$  is the effective height of the column,  $D$  is

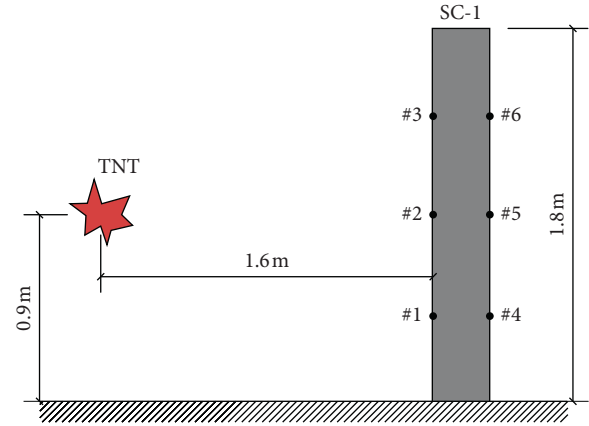


FIGURE 5: Measure points of SC-1.

the diameter of the column,  $t_f$  is the thickness of CFRP,  $M$  is the mass of TNT,  $H'$  is the height of TNT, and  $L$  is the distance between the column and TNT. The effective height of the circular column is 3500 mm, and the diameter is 400 mm. To facilitate the constraints, the top of the column is increased by 200 mm, while the actual height of the column is 3700 mm. The size of the RC base is 1000 mm × 1000 mm × 500 mm. The concrete strength grade is C40, and the reinforcement ratio is 0.9% (as shown in Figure 8).

In this test, four pressure transducers were installed on the front face of the specimens at different positions along the height of the column. The height of the four measure points were 330 mm, 1330 mm, 2330 mm, and 3300 mm, respectively. Three acceleration sensors were arranged on the back surface and their heights were 300 mm, 1750 mm, and 3300 mm, respectively. The sensor arrangements are shown in Figure 9.

Numerical simulation was based on Cases 25 and 27. The model was also generated according to the modelling methods mentioned in Section 2. Because the pressure sensor was damaged in the blast test, a small number of effective data were measured in the experiment. The numerical results were compared with those effective data. In Case 25, the arrival time of peak pressure measured from #2 pressure transducer was 2.56 ms and the peak pressure was 0.32 MPa. The results obtained from numerical simulation were 2.14 ms and 0.317 MPa, respectively. Additionally, Figure 10 shows the comparison between the experimental results and numerical analysis on #3 acceleration sensor. It can be learned from the above comparisons that the numerical analysis results were essentially in agreement with the experimental results. Thus, the linear elastic model for FRP and the multimaterial ALE method are applicable to predict the propagation of the blast wave and the blast response of reinforced concrete confined with FRP composite column.

**3.3. Equivalent Single-Degree-of-Freedom Model.** An equivalent single-degree-of-freedom model is a simplified method to study the dynamic deflection of structure [38]. Under blast loading, numerous vibration modes of the

TABLE 7: Comparison of experimental results and numerical simulation results (SC-1).

Measure point	Arrival time of blast wave (ms)			Peak value of blast wave (MPa)		
	Experiment	Simulation	Discrepancy (%)	Experiment	Simulation	Discrepancy (%)
#1	0.689	0.699	1.45	1.364	1.384	1.47
#2	0.515	0.499	3.11	6.202	5.726	7.67
#3	0.616	0.699	13.47	1.350	1.408	4.30
#4	1.169	1.099	5.99	0.361	0.365	1.11
#5	0.894	0.899	0.56	0.448	0.485	8.26
#6	1.296	1.099	15.2	0.401	0.366	8.73

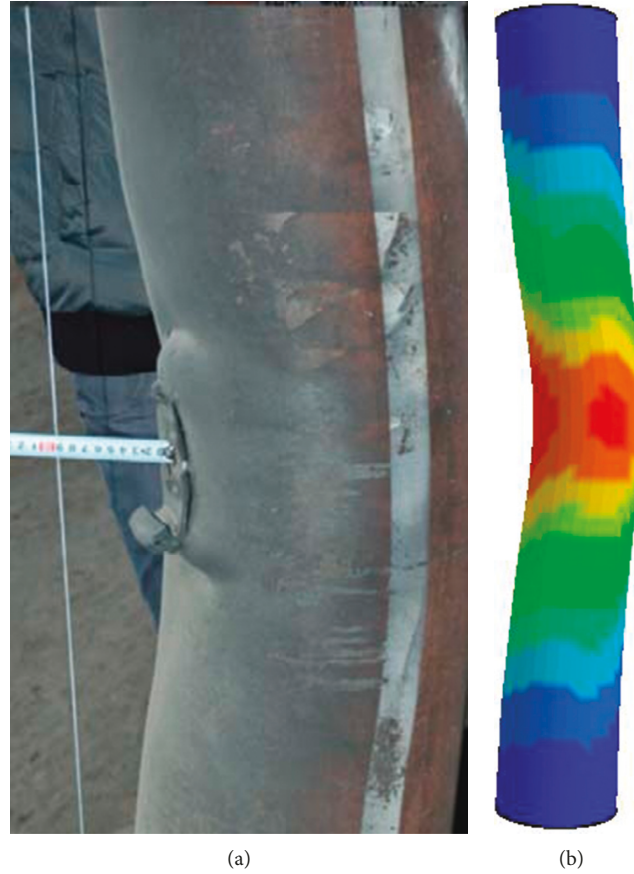


FIGURE 6: Damage mode of SC-2. (a) Experimental results. (b) Numerical results.

structural member will be generated. The domination mode of vibration can be considered as the deformation state of the member. The equivalent single-degree-of-freedom model (SDOF) was initially proposed by Norris et al. [39] and Biggs [40]. It replaces the motion state of the actual structure with the motion state of a concentrated mass spring. As illustrated in Figure 11, the structure is simplified to only one degree of freedom; that is, the mass of the structure is concentrated at a certain point, and then the point is limited to vibrate in a certain direction under dynamic loads. The equivalent mass ( $M_e$ ), equivalent load ( $F_e$ ), and equivalent stiffness ( $K_e$ ) can be obtained using the principle of energy conservation. The maximum dynamic displacement of the structure can be solved using the motion equation of the SDOF system. The motion equation of the ideal SDOF system ignoring the damping force is

$$M_e \ddot{y} + K_e y = F_e(t) \text{ (elastic stage)}, \quad (8a)$$

$$M_e \ddot{y} + R_e = F_e(t) \text{ (plastic stage)}, \quad (8b)$$

where  $y$  is the displacement of the equivalent system and  $R_e$  is the equivalent resistance. Adopting the load coefficient  $K_L = F_e/F$ , mass coefficient  $K_M = M_e/M$ , resistance coefficient  $K_R = R_e/R$ , and load-mass coefficient  $K_{LM} = K_M/K_L$ , the above motion equations can be rewritten as

$$K_{LM} M \ddot{y} + K_0 y = F(t) \text{ (elastic stage)}, \quad (9a)$$

$$K_{LM} M \ddot{y} + R_0 = F(t) \text{ (plastic stage)}, \quad (9b)$$

where  $K_0$  and  $R_0$  are the stiffness and resistance of actual structure, respectively.

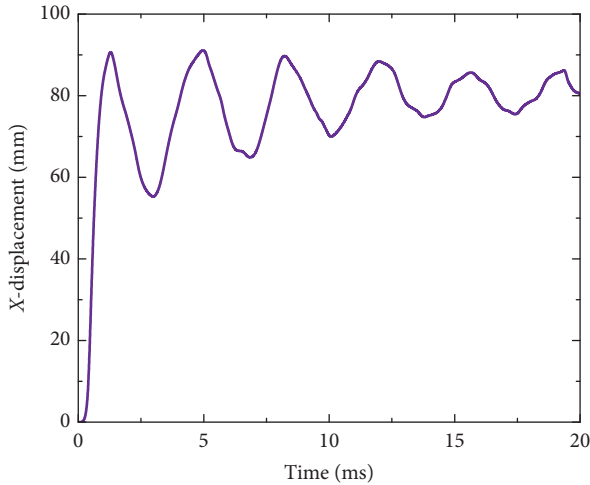


FIGURE 7: Displacement-time history curve of the midspan of SC-2.

TABLE 8: Four different cases of specimen JS5.

Case no.	$H$ (mm)	$D$ (mm)	$t_f$ (mm)	$M$ (kg)	$H'$ (m)	$L$ (m)
Case 24	3500	400	0.167	0.4	0.33	1.5
Case 25	3500	400	0.167	1	0.33	1.5
Case 26	3500	400	0.167	2	0.33	1.5
Case 27	3500	400	0.167	1	0.33	0

As to this study, the dynamic displacement of the proposed model in Section 2 was also calculated by the SDOF method to further verify the numerical model. Since the predicated column has two ends fixed, the coefficients of the system are shown in Table 9.

The resistance-deflection function for the SDOF system is illustrated in Figure 12 [41]. The maximum displacement in the elastic stage can be deduced as follows:

$$y_0 = \frac{R_e}{K_e} = \frac{K_R R_0}{K_L K_0} = \frac{R_0}{K_0}, \quad (10)$$

where  $R_0 = 16M_{pe}/L$ ,  $M_{pe}$  is the plastic limit bending moment,  $L$  is the length of the column, and  $K_0 = 307EI/L^3$ , where  $E$  and  $I$  are the elastic modulus and inertia moment, respectively.

According to blast resistance criteria of US Army, the maximum deflection of elastic-plastic SDOF system is given by [34]

$$y_m = \mu y_0, \quad (11)$$

where  $\mu$  is the factor which can be found in the empirical curve given by UFC-3-340-02. The maximum displacement of the predicated column is 23.36 mm after calculating by the SDOF method. The numerical result is 24.13 mm, which is in close agreement with the result of SDOF. The maximum displacement of numerical simulation is verified by the theoretical result.

In summary, the reliability of the finite element model is verified against the blast tests of CFST columns and reinforced concrete columns confined with FRP. The accuracy of numerical analysis in dynamic response under

blast loading is further confirmed by the SDOF result. In consequence, it is believed that the FE model developed in this paper can effectively predict the dynamic response of CFST columns confined with FRP under blast loading.

## 4. Results and Discussion

The proposed FE analysis model is rational from the above verification. After analysis and postprocessing, the dynamic response of a typical CFST column confined with FRP mentioned in Section 2 is discussed as follows.

**4.1. Displacement.** To study the displacement variation of the CFST column confined with FRP under blast loading, displacement contours in the direction of the  $X$ -axis (i.e., the propagation direction of the blast wave) at different times are shown in Figures 13 and 14, where Figure 13 is the front view and Figure 14 is the left view.

As seen from Figures 13 and 14 that when  $t = 0.4$  ms, the blast wave arrives at the column. The displacement at the middle of the column is relatively obvious, reaching 9.92 mm. As time goes on, the displacement of the column increases. When  $t = 0.9$  ms, the displacement of the column reaches the maximum value of 24.13 mm. When  $t = 2$  ms, the displacement in the middle of the column decreases and the displacements at both ends of the column increases. The displacement presents a symmetrical distribution with large middle and small ends for the whole.

Figure 15 illustrates the displacement-time history curve of the midheight point (i.e., point A in Figure 2) of the CFST column confined with FRP under blast loading. It can be seen from the figure that no transverse displacement occurs within 0–0.2 ms of the explosion. During this period, the blast wave propagates in the air after the detonation. After 0.2 ms, the displacement increases rapidly along the propagation direction. The maximum lateral displacement is 24.13 mm at 0.9 ms. The displacement of the column subsequently decreases and vibrates approximately 12 mm.

**4.2. Effective Stress of Steel Tube.** The stress state of CFST column confined with FRP under blast loading is very complicated. The equivalent stress, or von Mises stress, is usually used to represent its stress characteristics. Figure 16 displays the effective stress contours of the CFST column confined with FRP at different times.

As seen from Figure 16, the stress of the column increases rapidly at 0.3 ms. The peak stress in middle part reaches 410.93 MPa, exceeding the static yield strength of the steel tube. As time goes on, the areas of greater stress extend from middle of the column to the two ends of the column gradually. At 1 ms and 2 ms, the stress in most of the elements of the middle and two end parts is among 303–377 MPa, which exceeds the static yield strength of the steel tube. However, the stress in the transition areas between the middle and two ends is relatively small and does not exceed the yield strength. At 3 ms, the stress in the middle and two end parts of the column decreases. The effective stress is generally distributed symmetrically above and below.

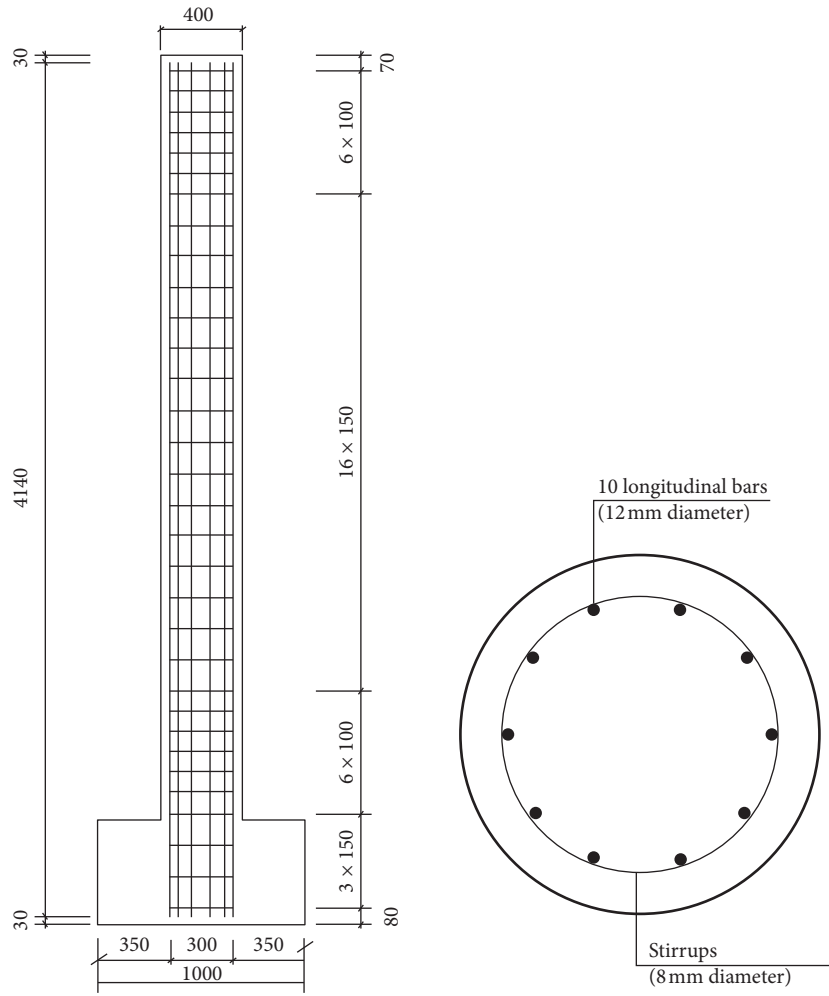
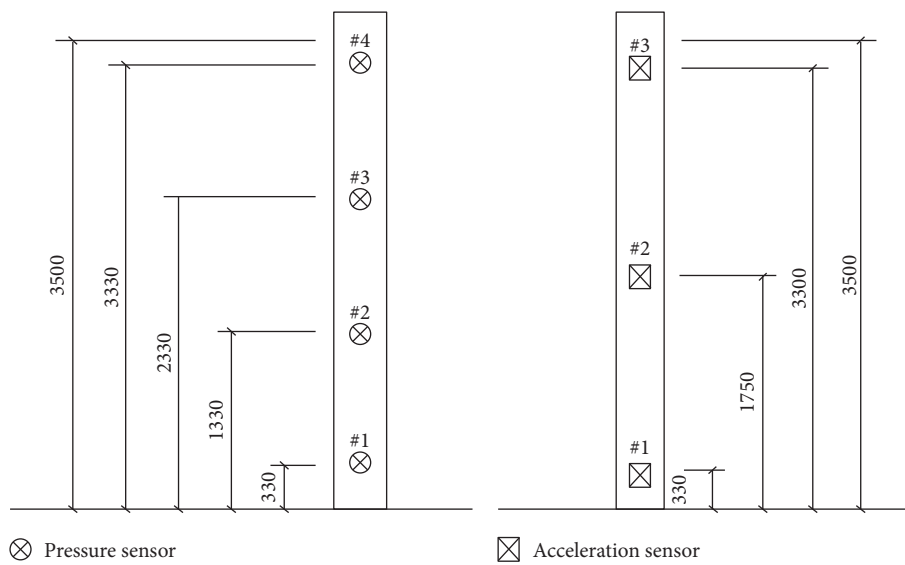


FIGURE 8: Geometry and reinforcement details of specimen JS5.



⊗ Pressure sensor

⊠ Acceleration sensor

FIGURE 9: Sensor arrangements of specimen JS5. (a) Pressure sensor. (b) Acceleration sensor.

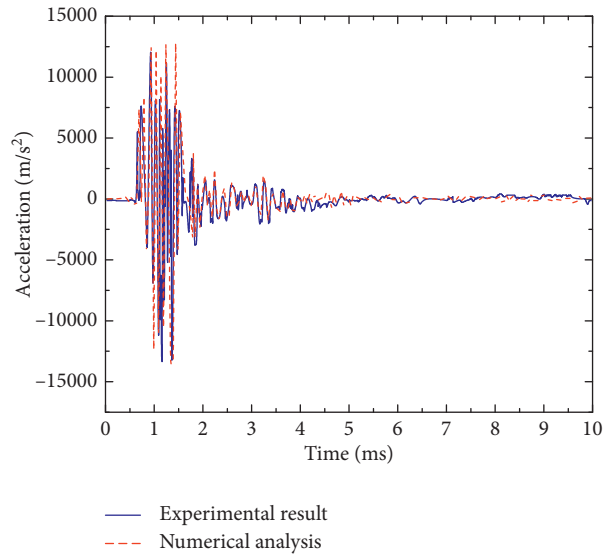


FIGURE 10: Acceleration-time history curve of #3 acceleration sensor.

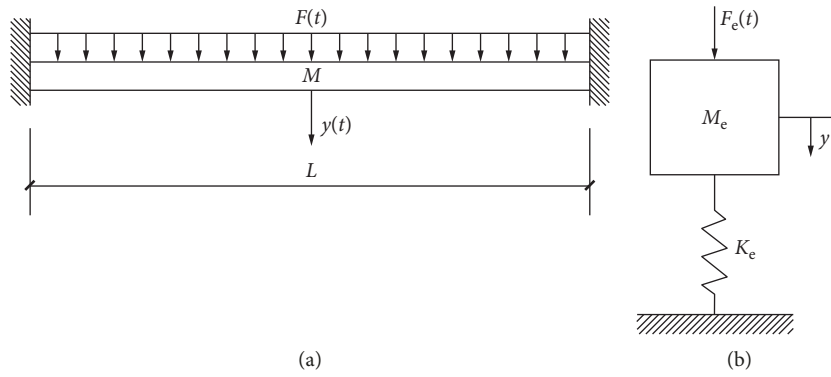
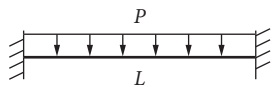


FIGURE 11: Equivalent single-degree-of-freedom model. (a) Actual structure. (b) Equivalent system.

TABLE 9: Conversion coefficients of the system.

Load and support condition	Stage	$K_L$	$K_M$	$K_{LM}$
	Elastic	0.53	0.41	0.77
	Elastic-plastic	0.64	0.50	0.78
	Plastic	0.50	0.33	0.66

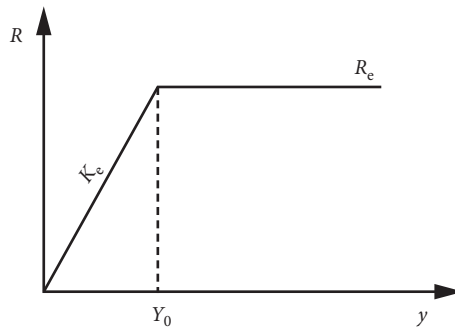


FIGURE 12: Resistance-deflection function.

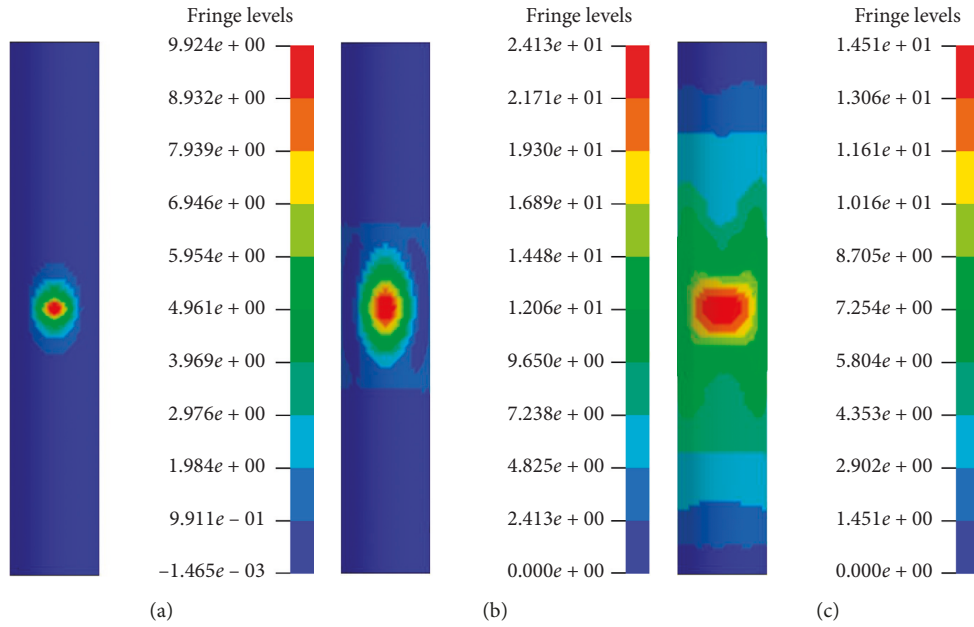


FIGURE 13: Contours of X-displacement at different time periods (front view): (a)  $t = 0.4$  ms, (b)  $t = 0.9$  ms and (c)  $t = 2$  ms.

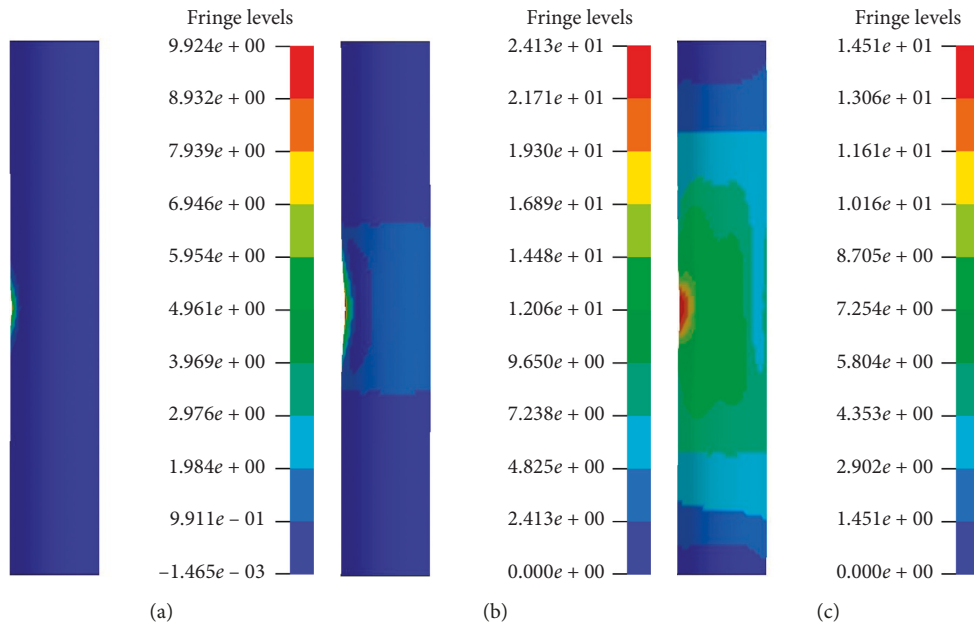


FIGURE 14: Contours of X-displacement at different time periods (left view): (a)  $t = 0.4$  ms, (b)  $t = 0.9$  ms, and (c)  $t = 2$  ms.

Therefore, the vulnerable parts of a CFST confined with FRP are the middle and two ends (Figure 17).

**4.3. Effective Stress of Concrete.** Figure 18 shows the effective stress contours of concrete at different times. Compared with the effective stress of the steel tube, the effective stress of the concrete is distributed evenly along the longitudinal member. In the initial stage, the effective stress of the concrete in the middle of the column increases rapidly, exceeding the static ultimate stress of concrete. The effective stress in other areas is relatively small and does not

exceed the ultimate stress. Due to the EROSION keywords, elements will be deleted if the strain value exceeds the failure strain. As time elapses, some elements in the middle section stop working first. Then, stress increases at the top and bottom of the column. These elements stop working, and shear failure occurs in the column. Stress in the middle part of the backside of the column increases gradually, and stress of most of the elements in this area is in the range of 44.06 MPa to 52.62 MPa, exceeding the static ultimate stress of the concrete. Thus, the vulnerable parts of the concrete are still the middle and two end parts of the column.

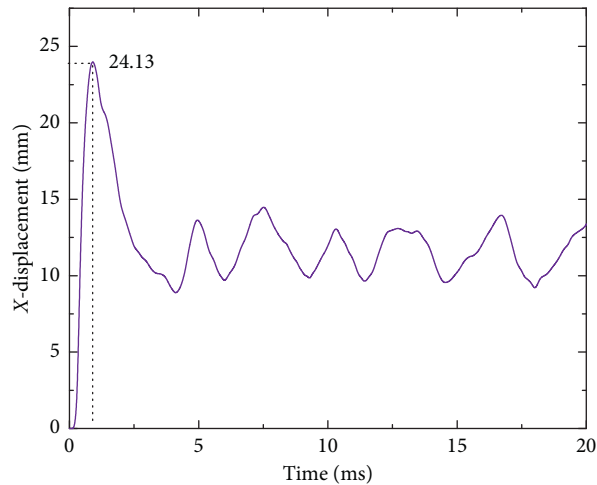


FIGURE 15: Displacement-time histories of the midheight point of CFSTs confined with FRP.

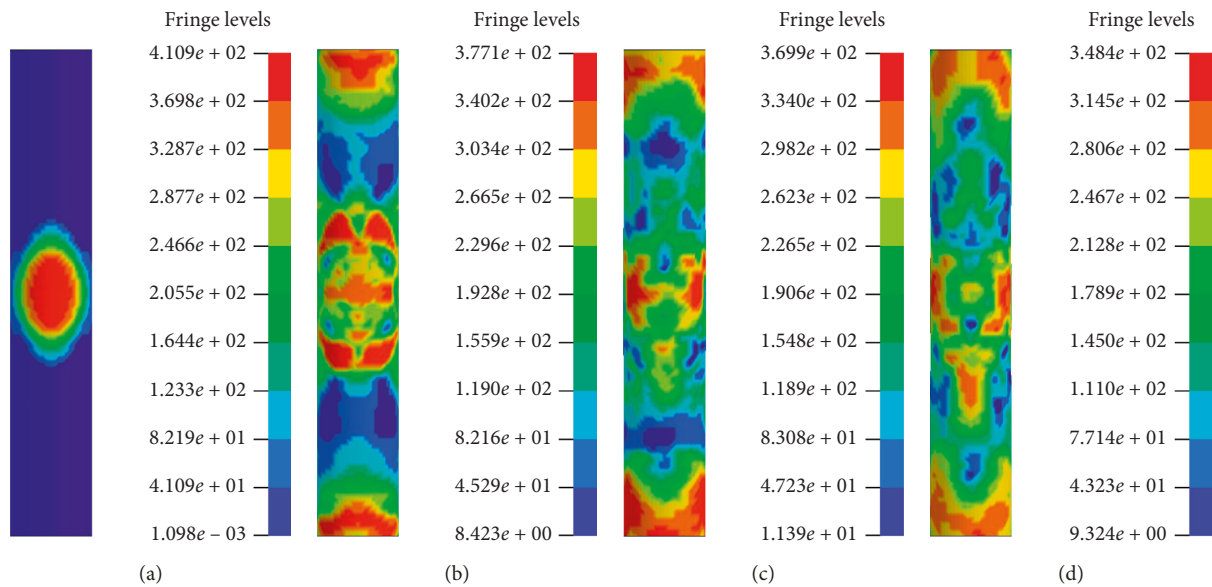


FIGURE 16: Effective stress contours of the steel tube at different time periods (front view): (a)  $t = 0.3$  ms, (b)  $t = 1$  ms, (c)  $t = 2$  ms, and (d)  $t = 3$  ms.

**4.4. Effective Stress of FRP.** The effective stress contours of FRP at different times are displayed in Figure 19. The stress distribution of FRP is similar to that of a steel tube. In the beginning, the area with higher stress is still the middle part of the column and later the stress at the two ends increases. The stress is higher in the middle part and two ends, while lower in the transition areas.

**4.5. Parametric Study**

**4.5.1. Number of FRP Layers.** To study the effect of number of FRP layers on the blast resistance of the CFST column confined with FRP, the dynamic response of the CFST columns confined with FRP with different layers under blast loading was simulated by changing the thickness of the FRP while keeping other parameters unchanged.

Figure 20 illustrates the displacement-time history curves of the CFST columns confined with FRP when the FRP is 0, 1, 2, 3, and 4 layers (the thicknesses of the FRP are 0, 0.167 mm, 0.334 mm, 0.501 mm, and 0.668 mm, respectively). When the number of FRP layers is 0, namely, a traditional CFST without the FRP constraint, the maximum displacement of the member under blast loading is 30.17 mm. When the number of FRP layers is 1, the maximum displacement of the column is 24.13 mm, a reduction of 6.04 mm compared with a nonretrofitted CFST column. It is found that the constraint of FRP could effectively improve the blast resistance of CFST columns. When the number of FRP layers is 2, 3, and 4, the maximum displacements are 22.11 mm, 19.52 mm, and 19.37 mm, respectively. This indicates that with an increase in the number of FRP layers, the blast resistance performance of the member is further improved, but its effect is

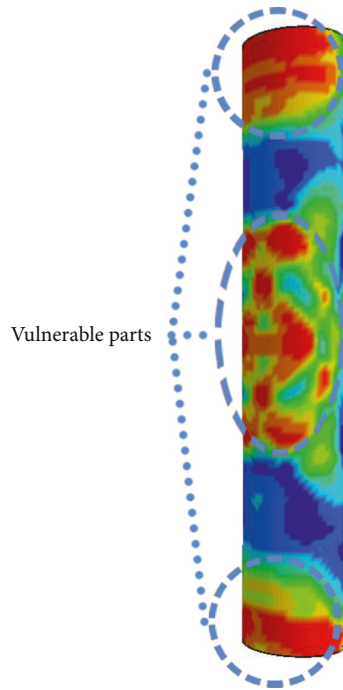


FIGURE 17: Vulnerable parts of the steel tube.

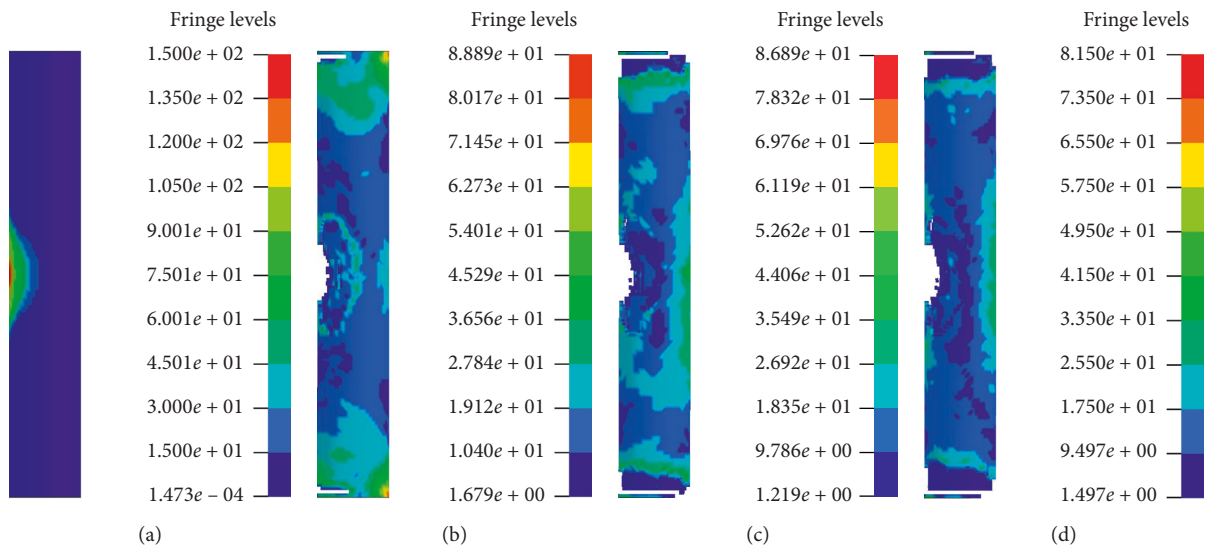


FIGURE 18: Effective stress contours of concrete at different time periods (left view): (a)  $t = 0.3$  ms, (b)  $t = 1$  ms, (c)  $t = 2$  ms, and (d)  $t = 3$  ms.

gradually weakened. As seen from the figure, the displacement of a three-FRP layer column and a four-FRP layer column is relatively close, but it is obvious that the three-FRP layer is more economical than the four-FRP layer.

**4.5.2. Concrete Strength.** The dynamic response of the CFST columns confined with FRP with four different concrete strength grades under the same blast loading is analysed while keeping the other parameters unchanged. The displacement-time history curves of the midheight point of the four cases are shown in Figure 21.

When the strength grades of the concrete are C35, C40, C45, and C50, the maximum displacements of the CFST columns confined with FRP are 28.32 mm, 24.13 mm, 21.65 mm, and 18.90 mm, respectively. The maximum displacement decreases gradually with an increase in the concrete strength grade. This indicates that the blast resistance of a CFST confined with FRP can be enhanced by improving the concrete strength.

**4.5.3. Cross Section.** In the engineering application, the CFST columns with the square section are more widely used because of its convenient joint connection. To study the

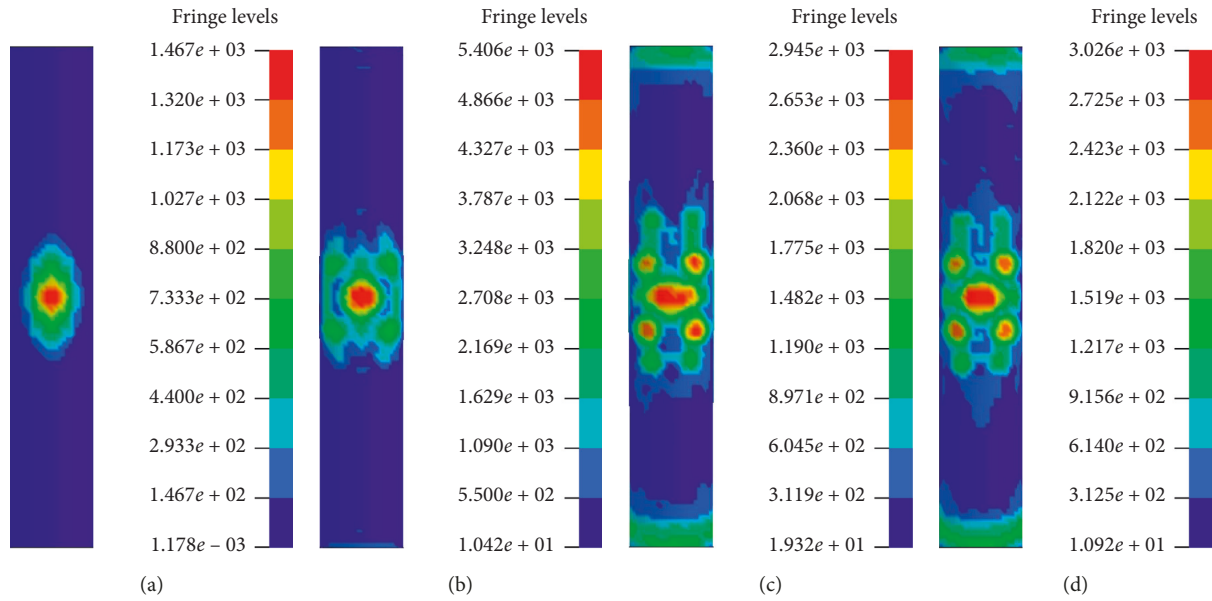


FIGURE 19: Effective stress contours of a steel tube at different time periods (front view): (a)  $t = 0.3$  ms, (b)  $t = 1$  ms, (c)  $t = 2$  ms, and (d)  $t = 3$  ms.

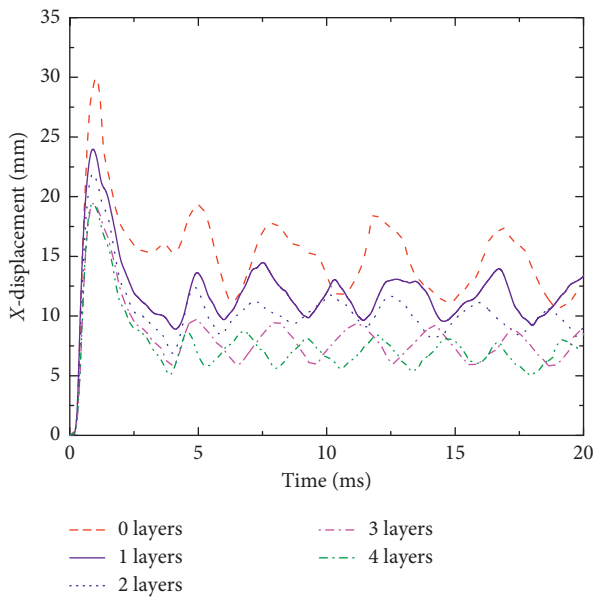


FIGURE 20: Comparison of midheight displacement with different thicknesses of FRP.

influence of the cross section on the blast resistance performance, two square-section column models are generated. One column is the same size with the circular one ( $500 \text{ mm} \times 500 \text{ mm} \times 3000 \text{ mm}$ ), and the other column is the same material consumptions with the circular one (namely, the section size is  $443 \text{ mm} \times 443 \text{ mm}$  and the thickness of steel tube is  $9 \text{ mm}$ ). The numerical results of the square section cases are compared with those of the circular section case. The displacement-time history curves of the two cases are shown in Figure 22.

Under the condition of the same section size, the maximum displacement of the square section column with

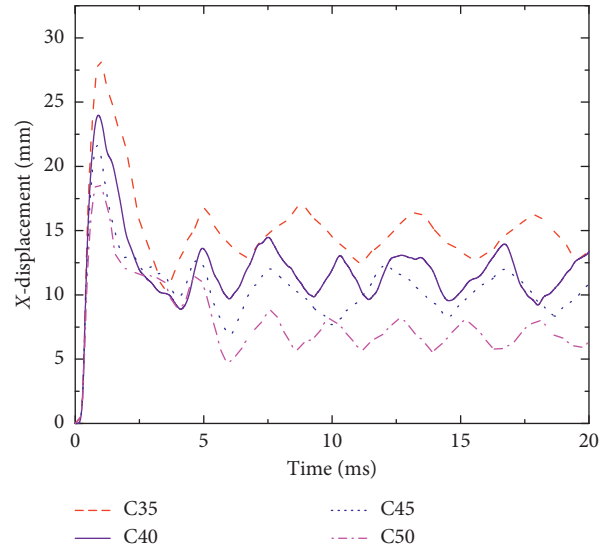


FIGURE 21: Comparison of midheight displacement with different comprehensive strengths of concrete.

the same section size is  $21.99 \text{ mm}$ , which is  $8.87\%$  less than that of the circular section member. The blast resistance performance of the square section member is better than that of the circular section member, but the square section member has  $27.39\%$  higher amounts of FRP, steel, and concrete than the circular member. Under the condition of the same material consumptions, the maximum displacement of the column with the square section is  $30.27 \text{ mm}$ . The column with circular section shows better blast performance than the one with square section. This is mainly because the circular section member has an excellent aerodynamic profile. Parts of the blast wave detours, and the impact energy reduces.

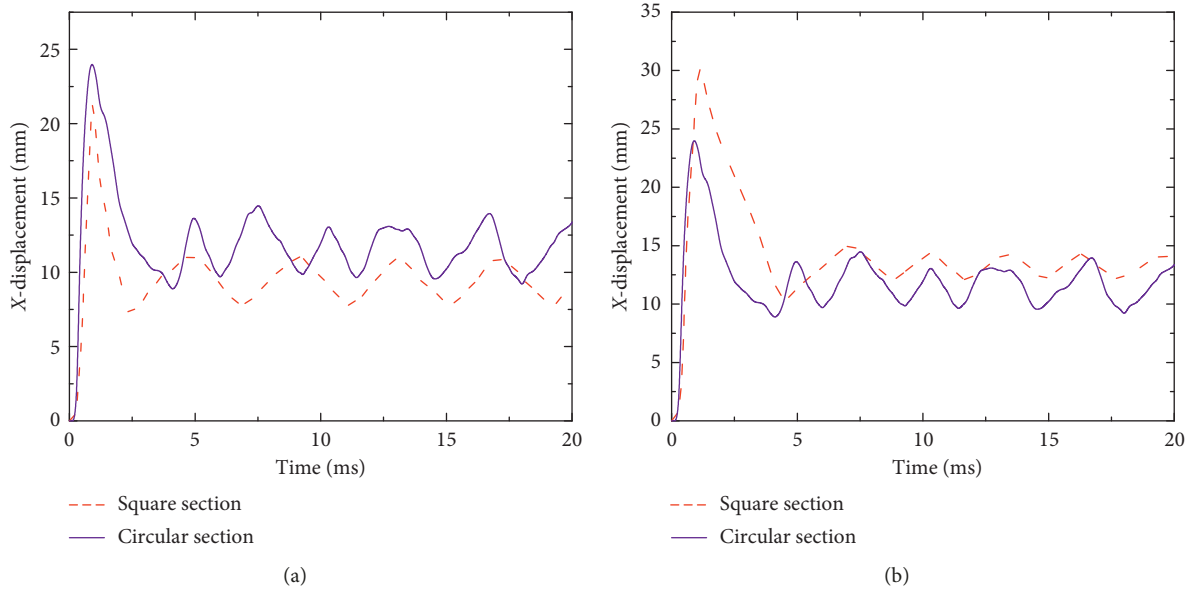


FIGURE 22: Comparison of midheight displacement with different cross sections. (a) Same section size. (b) Same material consumptions.

## 5. Conclusion

In this paper, the dynamic response of the CFST columns confined by FRP under blast loading was numerically investigated. Displacement, effective stress, and design parameters of a CFST confined with FRP were discussed in detail by using the developed finite element model, and the innovative conclusions based on these studies were summarized as follows:

- (1) Verified by the blast tests of CFST columns and RC columns confined with FRP and SDOF results, the FE model of the CFST column confined with FRP under blast loading using the multimaterial ALE method developed in this study is reliable to simulate the dynamic response. Using this method, the CFST column confined with FRP under blast loading with various scaled distances can further be modelled and analysed.
- (2) Under blast loading, the displacement of the column reaches the peak value in a short time and then drops to a certain range of vibration. When the scaled distance  $z$  is  $0.28 \text{ m/kg}^{1/3}$ , the maximum displacement is 24.13 mm and the deformation-span ratio is 0.8%. The CFST column confined with FRP performs a good blast resistance.
- (3) The stresses of the steel tube, concrete, and FRP generally show a symmetrical distribution. The stresses in the middle part and two ends of the column are higher, exceeding the static ultimate stress. The numerical results can provide a certain basis for blast protection of the CFST columns and a blast-resistance design of the CFST columns confined with FRP.
- (4) The stiffness and bearing capacity of the columns can be enhanced by increasing the number of FRP layers

or concrete strength. However, as the number of layers increases, the blast resistance enhancement effect decreases. When the number of layers is greater than 3 layers, it is of little significance to increase the layers for improving the blast resistance performance of the columns.

- (5) With the same cross section size, a column with a square cross section shows better blast resistance performance than the one with a circular cross section, but the materials consumptions are also greater. With the same materials, a column with a circular-section shows better blast performance than the one with a square cross section due to the wave detouring effect.

Further experimental study of CFST columns confined with FRP under blast loading is necessary to implement, and it will be one of our future works.

## Data Availability

The data used to support the findings of this study are available from the corresponding author upon request.

## Conflicts of Interest

The authors declare that they have no conflicts of interest regarding the publication of this paper.

## Acknowledgments

This study was financially supported by the National Natural Science Foundation of China (NSFC) (Grant nos. 51878056 and 51508028), Social Development Foundation for Science and Technology Planning Project of Shaanxi Province (Grant nos. 2019SF-256), Natural Science

Foundation of Shaanxi Province (Grant nos. 2018JQ5119 and 2018JQ5023), and Special Fund for Basic Scientific Research of the Central Colleges (Grant no. 300102288112).

## References

- [1] S. Morino, M. Uchikoshi, and I. Yamaguchi, "Concrete-filled steel tube column system-its advantages," *International Journal of Steel Structures*, vol. 1, no. 1, pp. 33–44, 2001.
- [2] J. Zeghiche and K. Chaoui, "An experimental behaviour of concrete-filled steel tubular columns," *Journal of Constructional Steel Research*, vol. 61, no. 1, pp. 53–66, 2005.
- [3] B. Uy, Z. Tao, and L.-H. Han, "Behaviour of short and slender concrete-filled stainless steel tubular columns," *Journal of Constructional Steel Research*, vol. 67, no. 3, pp. 360–378, 2011.
- [4] L. Van den Einde, L. Zhao, and F. Seible, "Use of FRP composites in civil structural applications," *Construction & Building Materials*, vol. 17, no. 6-7, pp. 389–403, 2003.
- [5] T. Uomoto, H. Mutsuyoshi, F. Katsuki, and S. Misra, "Use of fiber reinforced polymer composites as reinforcing material for concrete," *Journal of Materials in Civil Engineering*, vol. 14, no. 3, pp. 191–209, 2002.
- [6] Y. Xiao, W. H. He, and K.-K. Choi, "Confined concrete-filled tubular columns," *Journal of Structural Engineering*, vol. 131, no. 3, pp. 488–497, 2005.
- [7] Z. Tao and L.-H. Han, "Behaviour of fire-exposed concrete-filled steel tubular beam columns repaired with CFRP wraps," *Thin-Walled Structures*, vol. 45, no. 1, pp. 63–76, 2007.
- [8] Z. Tao, L.-H. Han, and L.-L. Wang, "Compressive and flexural behaviour of CFRP-repaired concrete-filled steel tubes after exposure to fire," *Journal of Constructional Steel Research*, vol. 63, no. 8, pp. 1116–1126, 2007.
- [9] Z. Tao, L.-H. Han, and J.-P. Zhuang, "Cyclic performance of fire-damaged concrete-filled steel tubular beam-columns repaired with CFRP wraps," *Journal of Constructional Steel Research*, vol. 64, no. 1, pp. 37–50, 2008.
- [10] L. Liu and Y. Lu, "Axial bearing capacity of short FRP confined concrete-filled steel tubular columns," *Journal of Wuhan University of Technology-Materials Science Edition*, vol. 25, no. 3, pp. 454–458, 2010.
- [11] J. W. Park, Y. K. Hong, and S. M. Choi, "Behaviors of concrete filled square steel tubes confined by carbon fiber sheets (CFS) under compression and cyclic loads," *Steel & Composite structures*, vol. 10, no. 2, pp. 187–205, 2010.
- [12] M. C. Sundarraja and G. G. Prabhu, "Investigation on strengthening of CFST members under compression using CFRP composites," *Journal of Reinforced Plastics and Composites*, vol. 30, no. 15, pp. 1251–1264, 2011.
- [13] M. C. Sundarraja and G. Ganesh Prabhu, "Finite element modelling of CFRP jacketed CFST members under flexural loading," *Thin-Walled Structures*, vol. 49, no. 12, pp. 1483–1491, 2011.
- [14] M. C. Sundarraja and G. Ganesh Prabhu, "Experimental study on CFST members strengthened by CFRP composites under compression," *Journal of Constructional Steel Research*, vol. 72, no. 5, pp. 75–83, 2012.
- [15] M. I. Alam, S. Fawzia, and X.-L. Zhao, "Numerical investigation of CFRP strengthened full scale CFST columns subjected to vehicular impact," *Engineering Structures*, vol. 126, pp. 292–310, 2016.
- [16] M. I. Alam, S. Fawzia, X.-L. Zhao, A. M. Remennikov, M. R. Bambach, and M. Elchalakani, "Performance and dynamic behaviour of FRP strengthened CFST members subjected to lateral impact," *Engineering Structures*, vol. 147, pp. 160–176, 2017.
- [17] C. Chen, Y. H. Zhao, and J. Li, "Experimental investigation on the impact performance of concrete-filled FRP steel tubes," *Journal of Engineering Mechanics*, vol. 141, no. 2, article 04014112, 2015.
- [18] V. S. Bindiganavile, *Dynamic fracture toughness of fiber reinforced concrete*, Ph.D. thesis, University of British Columbia, Vancouver, Canada, 2003.
- [19] P. A. Buchan and J. F. Chen, "Blast resistance of FRP composites and polymer strengthened concrete and masonry structures—a state-of-the-art review," *Composites Part B: Engineering*, vol. 38, no. 5-6, pp. 509–522, 2007.
- [20] A. A. Mutalib and H. Hao, "Numerical analysis of FRP-composite-strengthened RC panels with anchorages against blast loads," *Journal of Performance of Constructed Facilities*, vol. 25, no. 5, pp. 360–372, 2011.
- [21] L. Mao, S. Barnett, D. Begg, G. Schleyer, and G. Wight, "Numerical simulation of ultra high performance fibre reinforced concrete panel subjected to blast loading," *International Journal of Impact Engineering*, vol. 64, pp. 91–100, 2014.
- [22] F. Zhang, C. Wu, H. Wang, and Y. Zhou, "Numerical simulation of concrete filled steel tube columns against blast loads," *Thin-Walled Structures*, vol. 92, pp. 82–92, 2015.
- [23] Livermore Software Technology Corporation, *LS-DYNA Keyword User's Manual, Version 971*, Livermore Software Technology Corporation, Livermore, CA, USA, 2006.
- [24] G. R. Cowper and P. S. Symonds, "Strain hardening and strain rate effect in the impact loading of cantilever beams," *Small Business Economics*, vol. 31, no. 3, pp. 235–263, 1957.
- [25] T. J. Holmquist, G. R. Johnson, and W. H. Cook, "A computational constitutive model for concrete subjected to large strains, high strain rates, and high pressure," in *Proceedings of the 14th International Symposium on Ballistics*, pp. 591–600, American Defense Preparedness Association, Québec City, Canada, September 1993.
- [26] G. R. Johnson and W. H. Cook, "Fracture characteristics of three metals subjected to various strains, strain rates, temperatures and pressures," *Engineering Fracture Mechanics*, vol. 21, no. 1, pp. 31–48, 1985.
- [27] E. Cadoni, K. Labibes, C. Albertini, M. Berra, and M. Giangrasso, "Strain-rate effect on the tensile behaviour of concrete at different relative humidity levels," *Materials and Structures*, vol. 34, no. 1, pp. 21–26, 2001.
- [28] E. Ghorbi, M. Soltani, and K. Maekawa, "Development of a compressive constitutive model for FRP-confined concrete elements," *Composites Part B: Engineering*, vol. 45, no. 1, pp. 504–517, 2013.
- [29] J.-W. Nam, H.-J. Kim, S.-B. Kim, J.-H. Jay Kim, and K. J. Byun, "Analytical study of finite element models for FRP retrofitted concrete structure under blast loads," *International Journal of Damage Mechanics*, vol. 18, no. 5, pp. 461–490, 2009.
- [30] Committee Euro-International du Beton, *CEB-FIP Model Code 1990*, Thomas Telford Services Ltd., Lausanne, Switzerland, 1993.
- [31] L. J. Malvar, "Review of static and dynamic properties of steel reinforcing bars," *ACI Materials Journal*, vol. 95, no. 6, pp. 609–616, 1998.
- [32] H. Kimura, M. Itabashi, and K. Kawata, "Mechanical characterization of unidirectional CFRP thin strip and CFRP cables under quasi-static and dynamic tension," *Advanced Composite Materials*, vol. 10, no. 2-3, pp. 177–187, 2001.

- [33] A. A. Mutalib and H. Hao, "Development of P-I diagrams for FRP strengthened RC columns," *International Journal of Impact Engineering*, vol. 38, no. 5, pp. 290–304, 2011.
- [34] UFC 3-340-02, *Structures to Resist the Effects of Accidental Explosions*, United States Department of the Army, Washington, DC, USA, 2008.
- [35] S. F. Gong, H. Deng, S. B. Zhu, and W. L. Jin, "Numerical simulation for dynamic failure of a reinforced concrete slab under close-in explosion," *Journal of Vibration and Shock*, vol. 31, no. 2, pp. 20–24, 2012.
- [36] S. S. Sun, J. H. Zhao, S. H. He et al., "Dynamic response of concrete-filled steel tube piers under blast loadings," *Engineering Mechanics*, vol. 35, no. 5, pp. 27–35, 2018.
- [37] L. Liu, "Experimental study of differently protective RC piers under blast loading," Master thesis, Southeast University, Nanjing, China, 2016.
- [38] Y. Qasrawi, P. J. Heffernan, and A. Fam, "Performance of concrete-filled FRP tubes under field close-in blast loading," *Journal of Composites for Construction*, vol. 19, no. 4, article 04014067, 2015.
- [39] G. H. Norris, R. J. Hansen, M. J. Holly et al., *Structural Design for Dynamic Loads*, McGraw-Hill Book Co., New York, NY, USA, 1959.
- [40] J. M. Biggs, *Introduction to Structural Dynamics*, McGraw-Hill Book Co., New York, NY, USA, 1959.
- [41] L. Liu, Z. H. Zong, B. Tang, and M. Li, "Damage assessment of an RC pier under noncontact blast loading based on P-I curves," *Shock and Vibration*, vol. 2018, Article ID 9204036, 12 pages, 2018.

